Accepted manuscript (author version)

To appear in:

Iranian Journal of Catalysis (IJC)

Online ISSN: 2345-4865 Print ISSN: 2252-0236

Received: 05 September 2025

Revised: 08 February 2026

Accepted: 14 February 2026

Published Online: 07 April 2026

DOI: 10.57647/ijc.2026.1602.14

RESEARCH PAPER

Effect of Hematite Crystallinity on Catalytic Performance in the Heterogeneous Photo-Fenton Degradation of *para*-Nitrophenol

Swastika Pitahaya Novianiti (0009-0002-6407-7229)[1], Nurul Hidayat Aprilita (0000-0002-2132-6646)[1*], and Endang Tri Wahyuni (0000-0002-0584-0549)[1]

[1]Department of Chemistry, Universitas Gadjah Mada, Faculty of Mathematics and Natural Sciences, Bulaksumur, Yogyakarta 55281, Indonesia

*corresponding author, email: nurul.hidayat@ugm.ac.id

Abstract

This study explores the effect of hematite (α-Fe_2O_3) crystallinity on the heterogeneous photo-Fenton degradation of para-nitrophenol (PNP). Hematite was synthesized by precipitating $FeCl_3$ with NaOH, followed by oven drying at 100°C and calcination at 250°C and 500°C to obtain catalysts with different crystallinity levels. The degradation was carried out under UV irradiation in the presence of H_2O_2 and hematite, with optimization of catalyst dosage, H_2O_2 concentration, initial pH, and irradiation time. The catalysts were characterized by XRF, XRD, BET, FTIR, and UV-Vis DRS. XRD and FTIR confirmed that higher calcination temperatures promoted crystallinity and phase purity, while BET analysis showed that elevated temperatures reduced surface area due to particle growth and sintering. UV-Vis DRS revealed band gap narrowing with increased crystallinity. Among the catalysts, hematite calcined at 250°C displayed moderate crystallinity, mesoporosity (2.9 nm), and the largest surface area (70.89 m^2/g), achieving the highest PNP degradation (98.89%) at pH 6. In contrast, the oven-dried and highly crystalline (500°C) hematite exhibited lower catalytic performance. The 250°C catalyst also showed stability with minimal Fe leaching. These results highlight that moderate crystallinity optimizes catalytic activity and demonstrate the potential of engineered hematite as an efficient and reusable catalyst for sustainable water treatment.

Keywords: Hematite, Heterogeneous catalyst, Photodegradation, Photo-Fenton, *Para*-nitrophenol

1. Introduction

The presence of *para*-nitrophenol (PNP) in the environment can originate from the discharge of wastewater from industries such as pesticides, insecticides, herbicides, explosives, synthetic dyes, and pharmaceuticals [1]. PNP in aquatic environments is toxic to aquatic organisms and leads to environmental damage. Moreover, the accumulation of PNP in the human body can cause kidney and liver damage, central nervous system dysfunction, and symptoms such as headaches, skin rashes, cyanosis, methemoglobinemia, drowsiness, and nausea [2]. Therefore, the removal of PNP from wastewater before it is released into the environment is essential to prevent these adverse effects.

An effective method for PNP removal is degradation into harmless small molecules such as CO_2 and H_2O [3]. Among the degradation methods available, the photo-Fenton process has been widely applied due to its ability to generate hydroxyl radicals (•OH), which are powerful oxidants capable of degrading stable organic compounds like PNP [1,4,5]. The photo-Fenton process involves a reaction between H_2O_2 and Fe^{2+} (known as Fenton's reagent) under UV irradiation, producing •OH radicals (Eq.1-3). This method has been extensively studied for organic wastewater treatment due to several advantages, including rapid reaction times, simple operation, ambient temperature and pressure conditions, and the use of environmentally friendly reagents such as iron and H_2O_2, which decompose into water and oxygen [3,6].

$$Fe^{2+} + H_2O_2 \rightarrow Fe^{3+} + \bullet OH + OH^- \quad (1)$$

$$Fe^{3+} + H_2O_2 \rightarrow Fe^{2+} + HO_2\bullet + H^+ \quad (2)$$

$$H_2O_2 + h\nu \rightarrow 2\bullet OH \quad (3)$$

However, the photo-Fenton process operates most efficiently at low pH (between 2.8 and 3.5) [7–9], and its effectiveness significantly decreases at higher pH levels. This limits its application in wastewater treatment, as most wastewater typically has a near-neutral pH. Furthermore, using the photo-Fenton process at neutral pH can lead to the formation of iron sludge, primarily in the form of $Fe(OH)_3$, as Fe^{3+} ions react with OH^- ions (Eq.4). This sludge increases water turbidity, obstructs light penetration, reduces degradation efficiency, and raises treatment costs [7,9–14].

$$Fe^{3+} + OH^- \rightarrow Fe(OH)_3 \quad (4)$$

To improve the photo-Fenton process at near-neutral pH, recent studies have replaced dissolved Fe^{2+} catalysts with solid iron oxides in what is known as the heterogeneous photo-Fenton process. The use of solid iron oxide catalysts prevents the formation of iron sludge, thus maintaining efficiency at neutral pH. Iron oxides used in this process include hematite (α-Fe_2O_3) [15–18], goethite (α-FeOOH) [19,20], and magnetite (Fe_3O_4) [21–25].

The iron ions are often bonded to hydroxide ions (OH^-) as a ligand and forming $\equiv Fe^{3+}–OH$ able to react with H_2O_2 to form $\equiv Fe^{2+}$ species and $\bullet OH$ (Eq. 5). Later, $\equiv Fe^{2+}$ species generated can further react with H_2O_2 oxidized into $\equiv Fe^{3+}$ and produce more $\bullet OH$ (Eq.6) [12].

$\equiv Fe^{3+}–OH + H_2O_2 \rightarrow \equiv Fe^{2+} + H_2O + HO_2\bullet$ (5)

$\equiv Fe^{2+} + H_2O_2 \rightarrow \equiv Fe^{3+}–OH + \bullet OH$ (6)

$\equiv Fe^{3+}–OH + HO_2\bullet \rightarrow \equiv Fe^{2+} + H_2O/OH^- + O_2$ (7)

In the presence of applied UV light (hv), the reaction will generate electrons (e^-) and holes (h^+) on the surface of iron oxides. This photochemical activation process can be represented in Eq. 8. The generated e^- can reduce $\equiv Fe^{3+}$ to $\equiv Fe^{2+}$ (Eq.9) and react with dissolved oxygen (O_2) to produce superoxide radicals ($\bullet O_2^-$) (Eq.10), while the h^+ can generate $\bullet OH$ (Eq.11). UV light also directly photolyze hydrogen peroxide (H_2O_2) to generate $\bullet OH$ (Eq.3) [12].

$Fe_2O_3 + hv \rightarrow Fe_2O_3\ (e^- + h^+)$ (8)

$\equiv Fe^{3+} + e^- \rightarrow \equiv Fe^{2+}$ (9)

$e^- + O_2 \rightarrow \bullet O_2^-$ (10)

$h^+ + H_2O \rightarrow \bullet OH + H^+$ (11)

Among iron oxide, hematite (α-Fe_2O_3) has shown the most promising performance in enhancing the photo-Fenton process at neutral pH [12], due to its thermodynamic stability and suitable band gap of 2.1–2.2 eV for photocatalytic applications. Hematite and other iron oxides have been tested in the photodegradation of various organic pollutants such as tetracycline [26], acid orange 7 [27], methylene blue [12], and rhodamine B [26]; however, recent studies have also demonstrated their potential for PNP degradation. Tiar et al. (2025) investigated the photocatalytic oxidation of 4-nitrophenol using various iron-containing clays, including hematite (Fe_2O_3), under UV irradiation in the presence of H_2O_2. Although hematite was primarily used as a comparison material, the study confirmed its ability to participate in radical-mediated degradation reactions through both hydroxyl ($\bullet OH$) and superoxide ($\bullet O_2^-$) species [28]. Similarly, Sun and Lemley (2011) reported the efficient degradation of PNP via a heterogeneous Fenton-like reaction catalyzed by nano-magnetite (Fe_3O_4), achieving over 90% removal efficiency and elucidating a detailed degradation pathway [29]. These findings indicate that several iron oxides, including hematite and magnetite, have already exhibited strong catalytic activity toward PNP degradation and should be considered in related discussions.

Moreover, the iron oxides used in previous studies were often expensive commercial chemicals [30], even though hematite can be synthesized easily. The synthesis process typically involves a calcination step at high temperature, which influences the crystallinity of the iron oxide. Crystallinity, in turn, can affect the specific surface area [31], both of which collectively determine the material's ability to generate hydroxyl radicals (•OH) critical for pollutant degradation [12]. However, to date, no studies have specifically evaluated the effect of synthesized hematite's crystallinity on its catalytic activity in heterogeneous photo-Fenton systems. Therefore, this study aims to fill that gap by investigating the relationship between the crystallinity of hematite controlled via calcination temperature variation and its catalytic activity in the photo-Fenton degradation of *para*-nitrophenol.

2. Materials and methods

2.1 Materials

The materials used in this study included iron(III) chloride hexahydrate ($FeCl_3·6H_2O$, ≥99%, Merck), iron(II) sulfate heptahydrate ($FeSO_4·7H_2O$, ≥99%, Merck), sodium hydroxide (NaOH, ≥98%, Merck), *para*-nitrophenol (PNP, ≥99%, Merck), hydrogen peroxide (H_2O_2, 30% w/w, Merck), and sulfuric acid (H_2SO_4, 95–98%, Merck). Technical materials such as Whatman filter paper No. 42 (110 mm), deionized water, and double-distilled water were also used in all experiments.

2.2 Instrumentation

The equipment used in this research included standard laboratory glassware, an analytical balance (Mettler Toledo ME 204), hot plate stirrer (Thermo Scientific Cimarec), oven (Kirin-190), furnace (Vulcan-130), muffle furnace (Barnstead Thermolyne), magnetic stirrer (Ultrasonic Krisbow), and a photocatalytic reactor equipped with UV lamps (Himawari, λ = 330–380 nm) and visible light lamps (Philips, λ = 400–680 nm, P = 36 W), as well as a pH meter (ATC). Characterization and analysis instruments included an X-ray Diffractometer (XRD, PANalytical: X'Pert PRO Series 2318, Cu source), X-ray Fluorescence (XRF, Rigaku NEX CG II), Fourier Transform Infrared Spectroscopy (FT-IR, IPRPrestige-21 Shimadzu), Surface Area Analyzer (SAA, Quantachrome Novatouch Lx4), Diffuse Reflectance UV-Visible Spectroscopy (DR-UV, Perkin Elmer 365+), Atomic Absorption Spectroscopy (AAS, Perkin Elmer Model 3110), and a UV-Visible Spectrophotometer (Thermo Scientific GENESYS 150).

2.3 Synthesis of hematite

Hematite catalysts were synthesized using a chemical precipitation method. An iron chloride solution was prepared by dissolving 4.0576 g of $FeCl_3·6H_2O$ in 100 mL of deionized water. A 2 M NaOH solution was then added dropwise under magnetic stirring until the pH reached 11. The reaction mixture was heated to 80°C for 3 hours. The resulting precipitate was separated by centrifugation and washed with deionized water and ethanol. The precipitate was then dried at 100°C and calcined at 250°C, and 500°C for 4 hours.

2.4 Characterization of hematite

The synthesized materials were characterized using XRD, XRF, FT-IR, SAA, DR-UV, AAS, and UV-Vis spectroscopy. XRD was used to determine the crystal structure and phase composition, as well as to estimate crystallite size and crystallinity influenced by the calcination temperature. XRF was employed to analyze elemental composition and assess purity and possible contamination. FT-IR was used to identify bond vibrations or functional groups to understand the chemical bonds formed during synthesis. SAA was used to determine the specific surface area to evaluate the effect of calcination temperature on morphology. DR-UV was used to assess the optical properties and band gap energy of the materials, providing insight into their light absorption and energy transitions. AAS was used to evaluate the possible contribution of dissolved Fe species in the reaction. UV-Vis spectroscopy was used to measure absorbance before and after *para*-nitrophenol photodegradation.

2.5 Photodegradation activity test of *para*-nitrophenol via photo-Fenton method

The photocatalytic degradation activity of *para*-nitrophenol using hematite via the photo-Fenton method was evaluated using a standard *para*-nitrophenol solution. Optimization of reaction conditions, including H_2O_2 concentration, catalyst mass, pH, and UV irradiation time, was carried out using the hematite catalyst calcined at 250°C. A reaction mixture was prepared by adding 13.4 mg of catalyst into 20 mL of a 10 mg/L *para*-nitrophenol solution, followed by 10 mL of 60 mmol/L H_2O_2. The mixture was continuously stirred under UV light in a reactor for 90 minutes. Although the reactor was equipped with both UV and visible light lamps, all photocatalytic experiments in this study were conducted under UV irradiation (λ = 330–380 nm, P = 36 W). The visible light source was not used in this work, as the focus was to evaluate the catalytic performance of hematite under UV-assisted photo-Fenton conditions. After the reaction, the catalyst was separated by centrifugation at 5000 rpm for 10 minutes and filtered using Whatman No. 42 filter paper. The filtrate was analyzed using a UV-Vis spectrophotometer to determine the absorbance before and after degradation.

The samples were treated under various conditions, including different H_2O_2 concentrations (20, 40, 60, 80, and 100 mmol/L), catalyst masses (6.7, 13.4, 20.1, 26.8, 32.5, and 40.2 mg), pH levels (2, 3, 4, 5, and 6), and UV irradiation times (30, 60, 90, 120, and 150 minutes). When one variable was varied, the others were kept constant. The effect of calcination temperatures (250°C, and 500°C) and oven-dried temperature 100°C on the degradation efficiency of *para*-nitrophenol was also investigated by weighing 13.4, 13.1 mg, and 13.7 mg of the respective catalysts, with the catalyst mass adjusted to maintain an equivalent amount of iron in all experiments rather than using an identical catalyst mass; the iron molar content was calculated in advance based on the Fe percentage obtained from XRF analysis to ensure equivalence. The best results under each condition were determined by calculating the highest degradation efficiency, which indicated the optimal condition.

2.6 Comparison between heterogeneous and homogeneous photo-Fenton

For the homogeneous system, a solution was prepared by mixing 10 mL of 20 mmol/L $FeSO_4 \cdot 7H_2O$ with 20 mL of 10 mg/L *para*-nitrophenol solution in a beaker, followed by the addition of 10 mL of 60 mmol/L H_2O_2. The pH was adjusted to 6. The solution was continuously stirred under UV irradiation for 120 minutes. Afterward, the sample was filtered and analyzed using a UV-Vis spectrophotometer.

2.7 Analysis of para-nitrophenol solution after photodegradation

The final concentration of *para*-nitrophenol was determined by measuring the absorbance before and after photodegradation. The maximum wavelength (λmax) was first determined using a standard solution of *para*-nitrophenol scanned from 200 to 450 nm at 1 nm intervals. The sample absorbance was measured by UV–Vis spectrophotometry and quantified using a calibration curve constructed from standard PNP solutions with concentrations of 2, 4, 6, 8, 10, and 12 ppm. The calibration curve exhibited good linearity within this concentration range and was described by the linear regression equation $y = 0.0674x + 0.003$ with $R^2 = 0.9999$. The corresponding regression equation was used to determine the PNP concentration after degradation. The degradation efficiency was calculated using Eq. (12), where C_0 is the initial PNP concentration and C is the final concentration after photodegradation.

$$E = ((C_0 - C) / C_0) \times 100\% \qquad (12)$$

3. Results and discussion

3.1 X-ray diffraction (XRD) analysis

X-ray diffraction (XRD) analysis was performed to assess the crystallinity of the synthesized materials based on their diffraction patterns. The XRD patterns of all samples (100°C, 250°C, and 500°C) are presented in Fig. 1

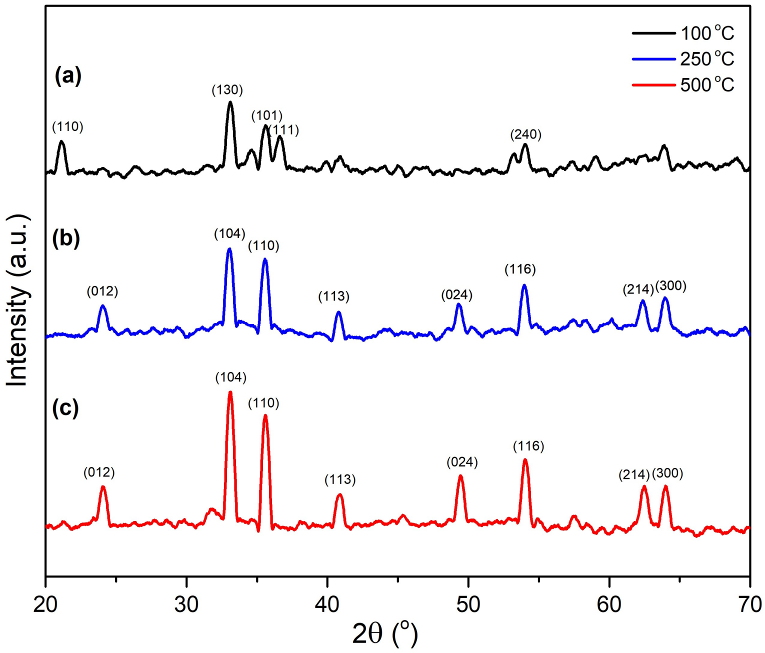

Fig. 1. XRD patterns of samples calcined at 100°C, 250°C, and 500°C

Fig. 1 shows the comparison of XRD patterns for the synthesized materials calcined at different temperatures. The pattern for the 100°C sample (Fig. 1a) displays several characteristic peaks of α-FeOOH at 2θ values of 21.14°, 33.11°, 35.56°, 36.63°, and 53.9°, corresponding to the (110), (130), (101), (111), and (240) planes of goethite with an orthorhombic structure (JCPDS No. 29-0713). This indicates that at 100°C, the material remained in the goethite phase and had not yet transformed into hematite. The broad and low-intensity diffraction peaks further suggest a low degree of crystallinity, indicating an early stage of crystal formation [32].

At 250°C (Fig. 1b), characteristic peaks of α-Fe_2O_3 begin to appear at 2θ values of 24.05°, 33.04°, 35.55°, 40.79°, 49.36°, 53.94°, 62.33°, and 63.9°, suggesting the transformation from goethite to hematite. These peaks are also observed for the sample calcined at 500°C (Fig. 1c) with very similar 2θ values. The diffraction patterns at both 250°C and 500°C match the rhombohedral hematite structure according to JCPDS No. 33-0664, with corresponding Miller indices (012), (104), (110), (113), (024), (116), (214), and (300). Compared to the 250°C sample, the diffraction peaks for the 500°C sample are sharper and narrower, indicating higher crystallinity due to more extensive crystal growth at elevated temperatures [31].

3.2 X-ray fluorescence (XRF) analysis

The powdered iron oxide samples was subjected to X-ray fluorescence (XRF) analysis showed in Table 1. The results indicate that iron (Fe) was the predominant element detected, with mass percentages of 82.92%, 83.78%, and 85.60% for the iron oxide samples 100°C, 250°C, and 500°C, respectively. These findings suggest a high iron content in the synthesized materials, consistent with the composition of hematite (Fe_2O_3). The increase in iron content with higher calcination temperature indicates that elevated temperatures facilitate the removal of volatile impurities, leading to higher purity of the iron oxide material [10]. It is important to note that the XRF instrument quantifies only detectable heavy elements (Fe, Cl, and Br) and does not detect oxygen. Consequently, the measured values are normalized to the detected elements and represent relative rather than absolute stoichiometric composition. This normalization explains the apparently higher Fe percentage compared to the theoretical Fe content in Fe_2O_3 (~70%). The data are thus used primarily to evaluate the relative variation in Fe and Cl among the samples. In addition to Fe, residual chlorine (14.3–16.8%) and minor bromine (<0.3%) were detected. The detected Cl does not correspond to unreacted $FeCl_3$ but to residual chloride species (e.g., Fe–Cl surface complexes or adsorbed Cl^-) that may remain after hydrolysis and calcination. The absence of $FeCl_3$ peaks in the XRD patterns confirms that no crystalline $FeCl_3$ remains. The dominance of Fe and the absence of precursor phases demonstrate that the synthesis successfully yielded phase-pure hematite (α-Fe_2O_3) suitable for catalytic applications.

Table 1. Elemental composition of synthesized iron oxide

Element	Mass (%)		
	100°C	250°C	500°C
Fe	82,92	83,78	85,6
Cl	16,82	15,96	14,3
Br	0,257	0,259	0,277

3.3 BET surface area analysis

The surface characteristics of the iron oxide samples were evaluated using nitrogen adsorption–desorption isotherms, as shown in Fig. 2. All samples exhibit Type IV isotherms with H3-type hysteresis loops according to the International Union of Pure and Applied Chemistry (IUPAC) classification, which are characteristic of mesoporous materials with slit-shaped pores [33,34]. As the calcination temperature increased, the isotherms became progressively flatter, and the adsorption volume decreased, particularly for the sample calcined at 500°C. This behavior indicates a significant reduction in mesoporosity, likely due to enhanced crystallinity leading to particle growth and partial pore collapse at elevated temperatures [35].

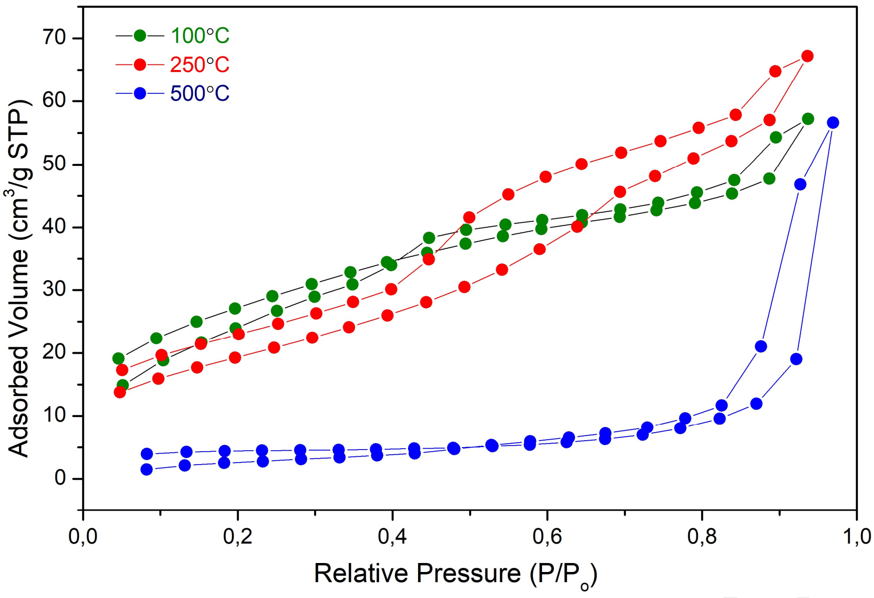

Fig. 2. N_2 adsorption–desorption isotherms of synthesized iron oxide

The specific surface area, pore volume, and average pore diameter for each sample are summarized in Table 2. Increasing the calcination temperature resulted in a marked decrease in both surface area and total pore volume from 98.07 m²/g and 0.09 cm³/g at 100°C to 13.17 m²/g and 0.08 cm³/g at 500°C while the average pore diameter remained within the mesoporous range. These findings highlight the critical role of calcination temperature in balancing crystallinity and surface properties to achieve optimal catalytic performance.

Table 2. BET specific surface area and pore characteristics of iron oxide samples calcined at different temperatures

Sample	Specific surface area (m^2g^{-1})	Pore volume (cm^3g^{-1})	Average pore diameter (nm)
100°C	98.07	0.09	1.81
250°C	70.89	0.10	2.94
500°C	13.17	0.08	13.29

As shown in Table 2, increasing the calcination temperature significantly reduces the surface area and total pore volume of the samples. The oven-dried material at 100°C has the highest surface area (98.07 m²/g), which is beneficial for catalytic applications due to the availability of more active sites. Meanwhile, the sample calcined at 500°C exhibits a drastically reduced surface area (13.17 m²/g), confirming the adverse effect of high-temperature calcination on porosity. Although the average pore diameter remains in the mesoporous range for all samples, the decline in surface area and pore volume at higher temperatures suggests that pore structure is compromised due to particle sintering and densification during crystal growth. These findings highlight the importance of controlling calcination temperature to balance crystallinity and surface properties for optimal catalytic performance.

3.4 Fourier-transform infrared (FTIR) analysis

Fourier-transform infrared (FTIR) spectroscopy was employed to identify functional groups and assess the phase transformation of synthesized iron oxide materials. The FTIR spectra (Fig. 3a–c) display absorption bands at ~3400, 1632, 1365, 928, 598, and 470 cm^{-1}. The broad band around 3400 cm^{-1} corresponds to O–H stretching vibrations from adsorbed water and hydroxyl groups in FeOOH, consistent with the XRD results. Peaks at 1632 cm^{-1} and 1365 cm^{-1} are attributed to bending vibrations of Fe–OH and physically bound water. The band at 928 cm^{-1} is associated with Fe–O–Fe stretching, while bands at 598 cm^{-1} and 470 cm^{-1} indicate Fe–O stretching and bending typical of hematite (α-Fe_2O_3) [36,37].

In the 100°C sample (Fig. 3a), additional bands at 803 and 893 cm^{-1} correspond to in-plane and out-of-plane bending modes (δ–OH and γ–OH) of Fe–OH, characteristic of goethite [38]. A band at 629 cm^{-1} also indicates the presence of Fe–O vibrations in goethite [39]. These findings suggest incomplete phase transformation, with abundant surface hydroxyl groups and adsorbed water, in agreement with the dominant goethite phase observed in XRD. At 250°C (Fig. 3b), reduced intensity of O–H related bands indicate ongoing dehydration and transformation from goethite to hematite. The appearance of a sharper Fe–O–Fe band and loss of goethite-specific bands further confirm the phase transition. By 500°C (Fig. 3c), Fe–O vibrations significantly intensify while O–H related bands nearly disappear, indicating complete dehydration and formation of well-crystallized hematite. This structural transition is expected to enhance the catalyst's stability and performance in heterogeneous photo-Fenton reactions at near-neutral pH.

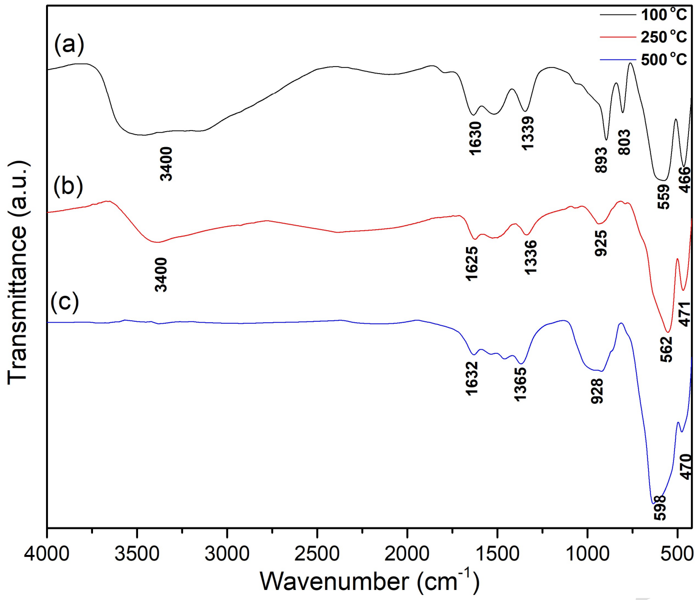

Fig. 3. FT-IR spectra of iron oxide with different calcination temperature

3.5 Optical Characterization via Diffuse Reflectance UV-Vis Spectroscopy

The optical properties of samples calcined at 100°C, 250°C, and 500°C (corresponding to FeOOH and α-Fe_2O_3 phases, respectively) were further analyzed using diffuse reflectance UV-Vis (DRUV-Vis) spectroscopy. The absorbance spectra of all samples (100°C, 250°C, and 500°C) are shown in Fig. 4.

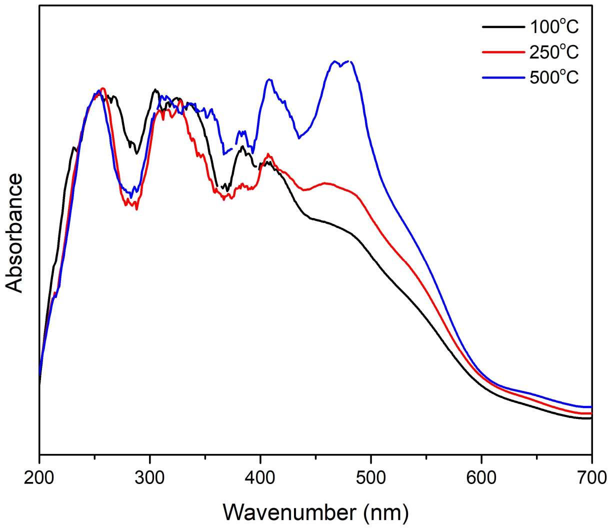

Fig. 4. Absorbance spectra of iron oxide samples

As shown in Figure IV.5, the samples calcined at 100°C, 250°C, and 500°C all absorb light in the visible region, particularly within the wavelength range of 450–700 nm. The highest visible light absorption was observed for sample calcined at 500°C, followed by 250°C and 100°C. This trend correlates with the increase in average crystallite size and degree of crystallinity. The ability to absorb visible light suggests that these iron oxides possess semiconductor-like structures characterized by their band gap energy (E_g) [40]. As the next step in determining the band gap energy (E_g), the diffuse reflectance data processed using the Kubelka-Munk function were analyzed through the Tauc plot method [41]. The Tauc plot visualization for the iron oxide samples is presented in Fig. 5.

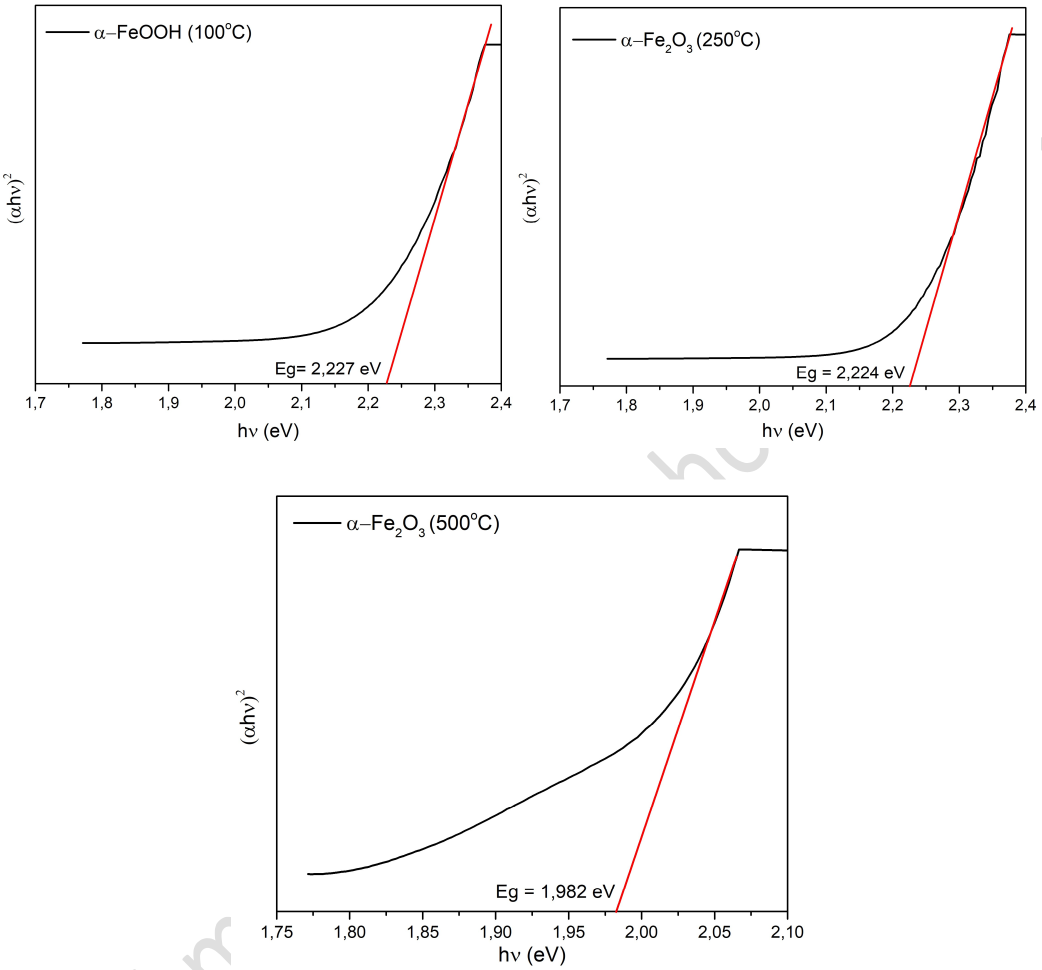

Fig. 5. Tauc plot of iron oxide

The calculated band gaps for samples at 100°C, 250°C, and 500°C were 2.227, 2.224, and 1.982 eV, respectively. These Eg values represent the energy separation between the valence and conduction bands in the semiconductor's electronic structure. The progressive narrowing of the band gap with increasing calcination temperature is attributed to microstructural changes, including particle growth and improved crystallinity. Higher temperatures enhance atomic coordination and reduce interatomic distances, facilitating electron excitation from the valence to conduction band by lowering the energy barrier [31,40,42]. Although the sample calcined at 500 °C exhibits a narrower band gap that is beneficial for light absorption, this advantage is counterbalanced by a drastic reduction in specific surface area caused by particle sintering and pore collapse at elevated temperatures.

The band gap value for sample calcined at 500°C (1.982 eV) aligns well with previously reported values, such as 1.93 eV [26], and theoretical band gap of Fe_2O_3 materials estimates in the range of 2.2 eV which also align with sample calcined at 250°C [12,43,44]. The 2.227 eV band gap obtained for sample calcined at 100°C is also consistent with the value reported by Liu et al. (2022) [45].

3.6 Heterogenous photo-Fenton with iron oxide as catalyst for PNP degradation

The photodegradation of PNP was used to evaluate the catalytic performance of iron oxide in heterogenous photo-Fenton reactions. The degradation efficiency is calculated by Eq.12, where C_0 is the initial concentration of PNP and C is the final concentration after PNP is degraded. The following factors are evaluated and discussed in this study as they affect the efficiency of the photo-Fenton processes. This includes catalyst dose, H_2O_2 concentration, solution pH, and irradiation duration.

3.6.1 The comparison between three different crystallinity

The influence of catalyst crystallinity on PNP photodegradation was investigated using sample calcined at 100°C, corresponds to FeOOH, while the 250°C and 500°C samples are hematite (Fe_2O_3) at doses of 13.7, 13.4, and 13.1 mg, respectively, in 10 mL of 60 mM H_2O_2 and 20 mL of 10 mg/L PNP at pH 3 and 6 for 120 minutes. The sample calcined at 250°C achieved the highest degradation efficiency (98.89%), outperforming those calcined at 100°C (94.44%) and 500°C (90.00%), indicating that crystallinity plays a key role in catalytic performance. Increasing calcination temperature progressively improved the crystallinity of the catalysts. The 100°C sample exhibited a poorly crystalline FeOOH structure, whereas the samples calcined at 250°C and 500°C showed the formation of well-crystallized α-Fe_2O_3. Higher crystallinity enhances charge mobility, thus improving photocatalytic efficiency. However, crystallinity alone does not determine activity. BET surface area values (Table 2) indicate that sample calcined at 100°C had the highest surface area (98.07 m^2/g), followed by 250°C at 70.89 m^2/g and 500°C at only 13.17 m^2/g. Despite its high surface area, sample calcined at 100°C exhibited lower activity due to inefficient charge transfer and limited pore size, which hinders PNP diffusion.

In contrast, sample calcined at 250°C, correspond to hematite, offered a favorable balance of surface area and pore size, facilitating PNP adsorption and degradation. At 500°C, although crystallinity increased, the drastic reduction in surface area and pore volume limited active site availability and decreased degradation efficiency. Overall, heterogeneous photo-Fenton performance depends on the synergy between crystallinity, surface area, and pore structure. α-Fe_2O_3 calcined at 250°C exhibited the most effective balance among these parameters, resulting in the highest photocatalytic performance and thus being used for the next operation conditions.

3.6.2 The effect of H_2O_2

The effect of H_2O_2 concentration, as shown in Fig. 6, revealed that the photodegradation efficiency of PNP increased as the H_2O_2 concentration rose from 20 mmol/L to 60 mmol/L. This enhancement can be attributed to the increased generation of hydroxyl radicals (•OH) through the photolytic decomposition of H_2O_2 under UV irradiation, where •OH plays a crucial role in the oxidative degradation of PNP. The highest degradation efficiency was observed at 60 mmol/L, indicating the optimal concentration of H_2O_2 for •OH production.

Beyond this optimal concentration, a decline in degradation efficiency was observed. This phenomenon can be explained by the scavenging effect of excess H_2O_2, which competes with PNP for reaction with •OH, thereby reducing the availability of reactive species required for effective degradation. As described in Eqs.13−14 [10,14,33,46,47], excessive H_2O_2 can act as a scavenger of •OH, leading to the formation of less reactive species such as HO_2• and ultimately lowering the degradation performance.

$$\bullet OH + H_2O_2 \rightarrow H_2O + HO_2\bullet \quad (13)$$

$$HO_2\bullet + \bullet OH \rightarrow H_2O + O_2 \quad (14)$$

For comparison, a control experiment using only H_2O_2 under UV irradiation (without the catalyst) resulted in 33.39% PNP degradation after 120 minutes. This indicates that some PNP removal can occur through direct photolysis of H_2O_2, which generates •OH radicals under UV light. Nevertheless, the much higher degradation efficiencies (above 94%) achieved with the catalysts clearly confirm that the heterogeneous photo-Fenton process is the dominant degradation pathway.

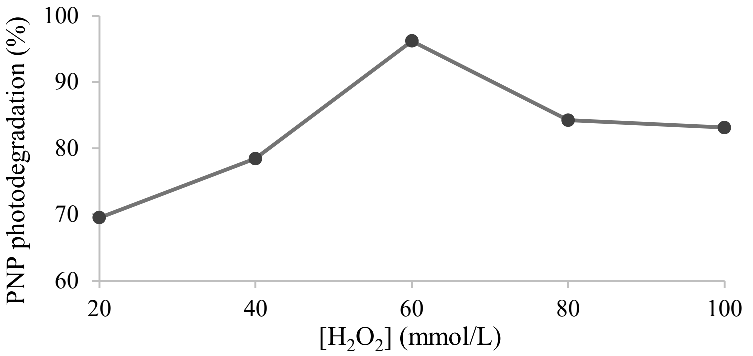

Fig. 6. The effect of H_2O_2 concentration on PNP photodegradation (mixture of 13,4 mg hematite, 10 mL H_2O_2, and 20 mL PNP 10 ppm at pH 6 for 90 minutes).

3.6.3 The effect on catalyst dose

The effect of catalyst dosage on PNP photodegradation, as shown in Fig. 7, indicates that degradation efficiency increased with the catalyst mass from 6.7 mg to 13.4 mg. This enhancement is attributed to the increased number of active sites on the catalyst surface, which promotes the generation of hydroxyl radicals (•OH) crucial for the oxidative degradation of PNP. The maximum degradation efficiency of 98.39% was achieved at 13.4 mg, identifying this as the optimal catalyst dosage. Beyond this point, further increases in catalyst mass did not result in significant improvements and instead led to a slight decline in efficiency. This decline can be explained by the saturation effect, where excess catalyst increases suspension turbidity, causing a shielding effect that hinders UV light penetration and reduces •OH generation [10,33,46,47]. Additionally, an excessive amount of catalyst may promote radical scavenging, as described in Eq. 15 [8,48,49]. This kind of behavior is characteristic of catalytic processes where optimum efficiency is achieved at the ideal catalyst dose.

$$\equiv Fe^{2+} + \bullet OH \rightarrow \equiv Fe^{3+} + OH^{-} \quad (15)$$

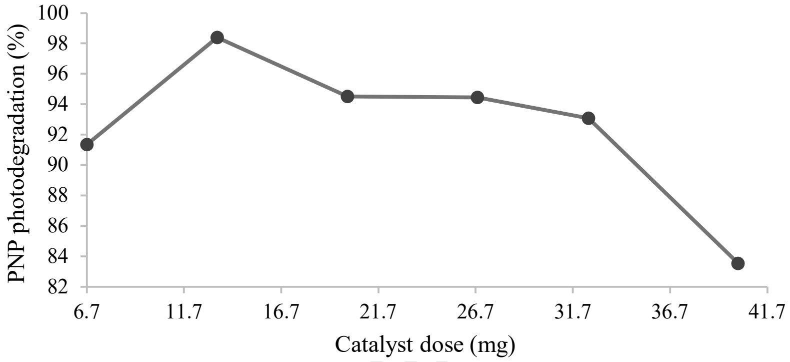

Fig. 7. The effect of the catalyst dose on PNP photodegradation (mixture of 10 mL H_2O_2 60 mmol/L and 20 mL PNP 10 ppm at pH 6 for 90 minutes).

3.6.4 The effect of solution pH

The influence of pH on the photodegradation efficiency of *para*-nitrophenol (PNP) is shown in Fig. 8. A significant increase in degradation was observed as the pH increased from 2 to 3, after which the efficiency remained relatively stable up to pH 7.

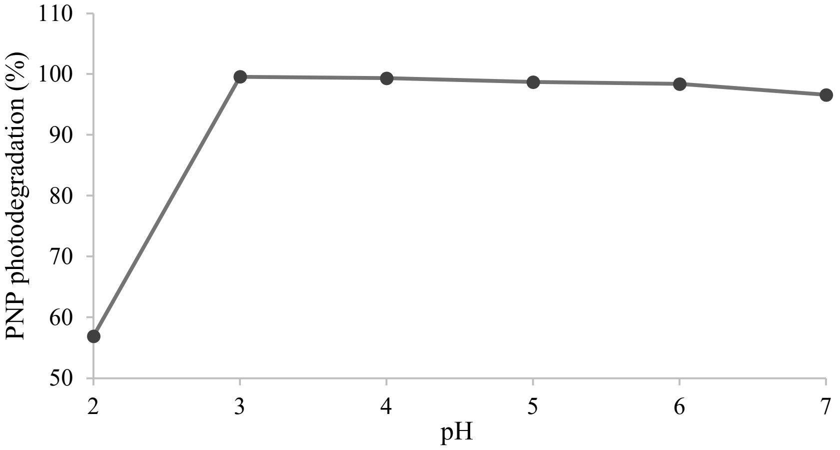

Fig. 8. The effect of solution pH on PNP photodegradation (mixture of 13,4 mg hematite, 10 mL H_2O_2 60 mmol/L and 20 mL PNP 10 ppm for 90 minutes).

At pH 2, degradation was minimal due to the excess H^+ ions scavenging •OH radicals and the formation of stable Fe-aquo complexes, which inhibit •OH generation [14,46,47]. In contrast, at pH 3, the availability of free Fe^{2+} and H_2O_2 led to increased •OH formation, and the neutral form of PNP (pKa = 7.15) interacted more readily with the positively charged catalyst surface, resulting in optimal degradation [14].

From pH 4 to 7, degradation remained high but slightly decreased, partly due to the decomposition of H_2O_2 [47]. Nonetheless, the catalyst surface retained a positive charge (pHpzc = 8), promoting interaction with neutral PNP via weak electrostatic attraction. This facilitated effective adsorption and subsequent degradation of PNP. This indicates that the heterogeneous photo-Fenton system using α-Fe_2O_3 (250 °C) catalyst operates effectively across a wider pH range compared to the conventional homogeneous system.

3.6.5 The effect of irradiation duration

The degradation process indicated that irradiation time plays a crucial role in photodegradation efficiency, as presented in Fig. 9. Initially, the efficiency increased significantly with longer irradiation, reaching its optimum at 120 minutes. Beyond this point, the efficiency showed a slight decline and then stabilized, indicating a plateau where extended exposure no longer enhances degradation. These conditions supported effective interaction between hematite, H_2O_2, and light, promoting the generation of •OH radicals for PNP degradation. The slight decrease in efficiency after the optimal irradiation time is likely due to the recombination of intermediate radicals (Eq. 13–14) or the depletion of H_2O_2 as the reactive species [12,14,50,51], which limited further degradation.

For comparison, a control test was conducted under dark conditions to evaluate the contribution of UV irradiation. In the absence of light (conventional Fenton reaction), the degradation of p-nitrophenol reached only 41.98% after 120 min, whereas the UV-assisted photo-Fenton system achieved 97.46% degradation under identical conditions. This demonstrates that UV illumination significantly accelerates the formation of hydroxyl radicals by promoting Fe^{3+} photoreduction to Fe^{2+}, thereby enhancing the overall catalytic activity. The result confirms that the photo-Fenton process provides a clear advantage over the conventional Fenton reaction in terms of degradation rate and efficiency.

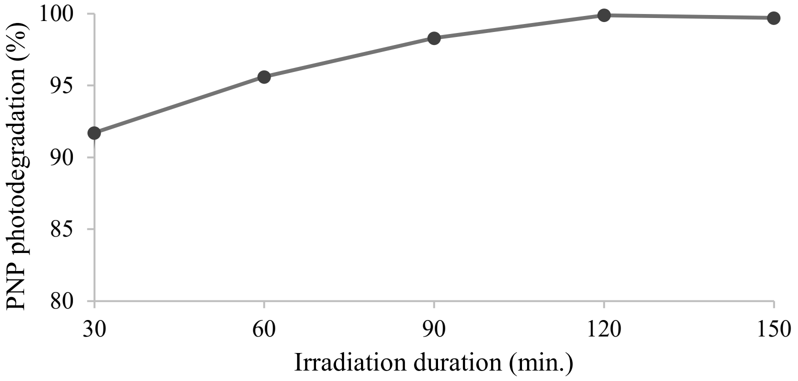

Fig.9. The effect of irradiation time on PNP photodegradation (mixture of 13,4 mg hematite, 10 mL H_2O_2 60 mmol/L and 20 mL PNP 10 ppm at pH 6).

3.7 Comparative behaviour between heterogeneous and homogeneous photo-Fenton

The photo-Fenton performance of homogeneous and heterogeneous systems was compared under identical conditions (Figure 10) using a Fe:H_2O_2 molar ratio of 1:3, 20 mL of 10 $mg\cdot L^{-1}$ PNP solution, and pH 3 and 6. As shown in Figure 10, at pH 3, the homogeneous system achieved 97.46% degradation, marginally lower than that of the heterogeneous system (99.6%). The high efficiency of the homogeneous reaction under acidic conditions is attributed to the stability and high reactivity of Fe^{2+} with H_2O_2, generating hydroxyl radicals (•OH) via the classical Fenton reaction. However, the homogeneous system is highly pH-dependent. At pH 6, Fe^{3+} precipitates as $Fe(OH)_3$, hindering the Fe^{2+}/Fe^{3+} redox cycle and reducing the degradation efficiency to 42.43%.

In contrast, the heterogeneous system exhibited high and stable performance across pH values. At pH 3, it reached 99.6% efficiency, driven by active surface sites that generate •OH and simultaneously facilitate valence band hole (h^+)-mediated degradation. Additionally, limited leaching of Fe^{2+}/Fe^{3+} under acidic conditions enhances •OH formation [10], while the positively charged catalyst surface promotes adsorption of neutral PNP molecules. At pH 6, the heterogeneous system maintained high efficiency (98.12%), outperforming the homogeneous counterpart. This stability is attributed to surface-bound Fe species that remain catalytically active despite the lower Fe solubility. Hydroxyl radical generation is sustained through H_2O_2 interaction with surface Fe sites and direct h^+ participation under UV light [10,52]. No $Fe(OH)_3$ precipitation occurs, as iron remains in a solid, catalytically active phase.

These results highlight the superior stability and efficiency of the heterogeneous photo-Fenton system, particularly at near-neutral pH, making it a promising and environmentally favorable alternative for real wastewater treatment without extensive pH adjustment. The degradation efficiencies were determined from the average of three independent experiments, with a standard deviation within ±2%. Therefore, the small difference between 97.46% and 99.6% degradation lies within the experimental error and is not statistically significant. This confirms the stability and reproducibility of the photo-Fenton system.

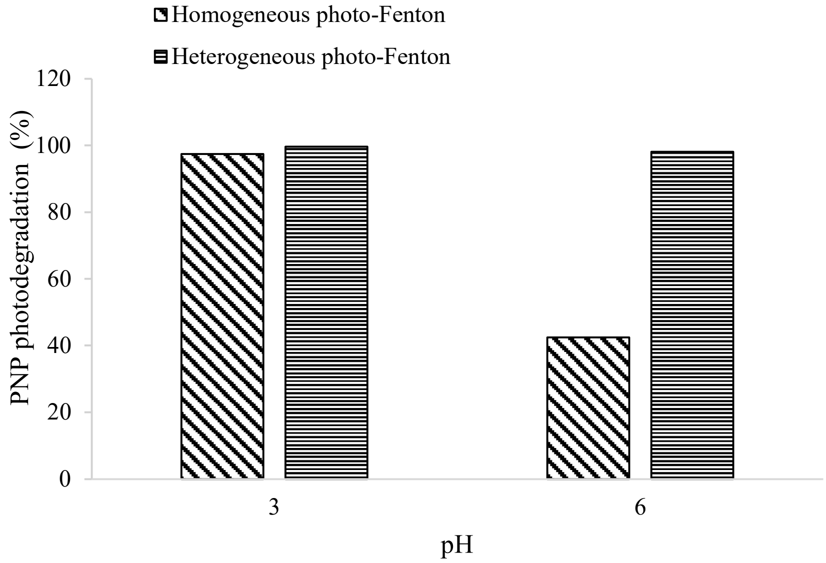

Fig.10. The comparation between heterogenous at pH 3 and pH 6, homogenous at pH 3 and pH 6 of PNP photodegradation

3.8 Characterization post-used photodegradation reaction

The stability of the α-Fe_2O_3 catalyst was assessed using XRD, FTIR, and AAS to monitor potential changes in crystal structure and iron leaching during the reaction. The XRD patterns (Fig. 11) of both fresh (a) and used (b) α-Fe_2O_3 catalysts revealed characteristic diffraction peaks at 2θ values of 24.09°, 33.11°, 35.59°, 40.81°, 49.42°, 54.00°, 62.39°, and 63.94°, corresponding to hematite planes based on JCPDS No. 33-0664. The absence of significant changes in the diffraction pattern after use indicates that the crystalline structure of α-Fe_2O_3 remained stable, confirming its potential for reuse in photo-Fenton applications.

FTIR spectra (Fig. 12) supported the XRD results, with Fe–O stretching bands at 554 and 471 cm^{-1} remaining evident after the reaction. However, new absorption bands appeared at 2923 and 2865 cm^{-1}, attributed to C–H stretching from organic residues, and at 2370 and 2335 cm^{-1}, possibly from adsorbed CO_2. Broadened bands at 3414 and 1649 cm^{-1} were associated with O–H and H–O–H stretching, indicating hydroxyl group presence. These changes suggest surface interactions between α-Fe_2O_3 and *para*-nitrophenol (PNP) molecules during the reaction, without compromising the hematite structure.

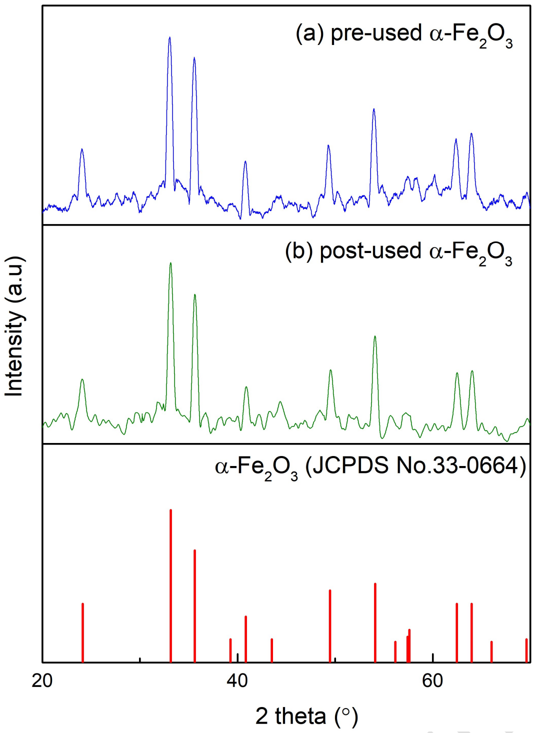

Fig. 11. The XRD patterns of hematite (a) pre-used and (b) post-used as photodegradation catalyst.

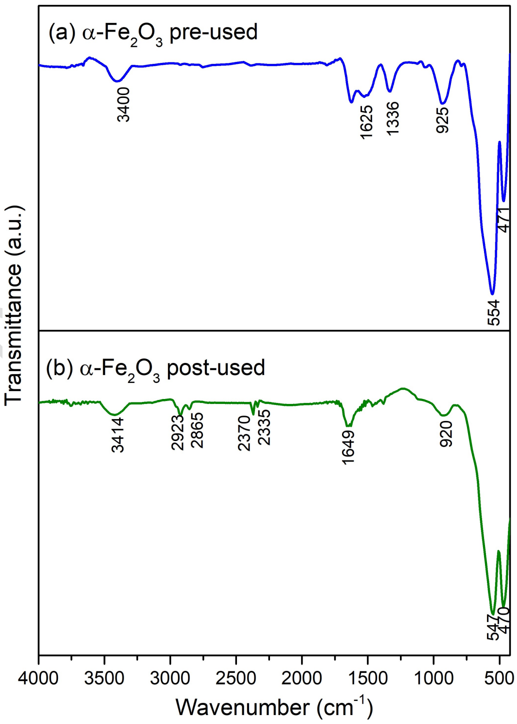

Fig.12. The FTIR patterns of hematite (a) pre-used and (b) post-used as photodegradation catalyst.

AAS analysis of dissolved Fe further evaluated the catalyst's chemical stability. As shown in Fig. 13, Fe dissolution increased up to 60 minutes and then decreased over time. The initial leaching likely resulted from redox interactions between the hematite surface and H_2O_2 or hydroxyl radicals [21]. Over time, Fe^{3+} ions may have reprecipitated as $Fe(OH)_3$ due to the availability of OH^- ions at near-neutral pH [53].

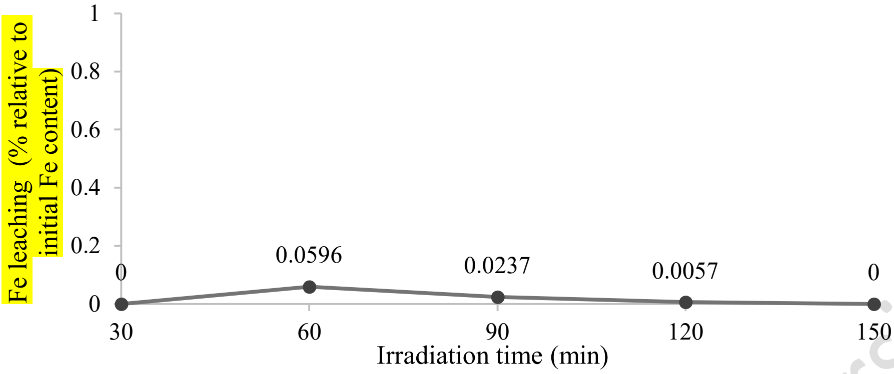

Fig.13. Percentage of Fe leached within various time

Fig. 14 indicates that Fe dissolution is highly pH-dependent, peaking at pH 2 and dropping significantly at higher pH values, consistent with the findings of Tiar et al. (2024) [1]. Thus, operating the photo-Fenton process with α-Fe_2O_3 under near-neutral pH conditions not only ensures structural stability but also minimizes iron leaching, supporting its environmentally friendly application in wastewater treatment.

The heterogeneous nature of the reaction was inferred from the excellent reusability and stable catalytic activity of the Fe_2O_3 catalyst. Although a specific hot-filtration test was not conducted in this study, the stable catalytic performance and unchanged color of the reaction solution suggest minimal Fe leaching during the reaction. Previous work by Demarchis et al. (2015), reported that Fe dissolution from hematite under photo-Fenton conditions was below 10 mg/L, with Fe mainly present as Fe^{3+} due to oxidation by H_2O_2 at acidic pH. These results indicate that the homogeneous contribution from dissolved Fe is negligible, and the system can be considered predominantly heterogeneous [54].

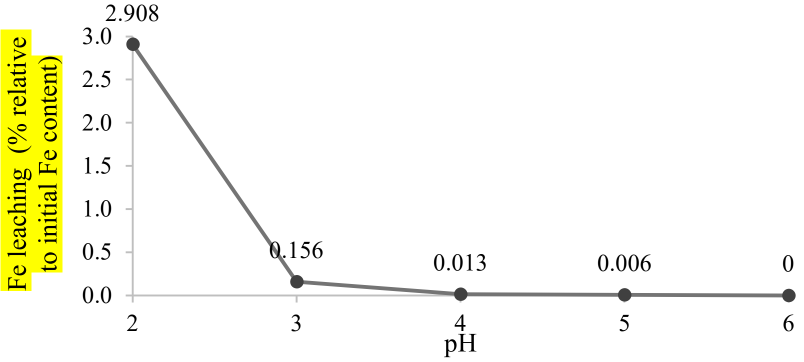

Fig.14. Percentage of Fe leached within various pH

4. Conclusion

This study introduces a temperature-tuned approach for synthesizing hematite (α-Fe_2O_3) catalysts with tailored crystallinity and surface characteristics through controlled calcination. Increasing the calcination temperature led to enhanced crystallinity and particle growth, while simultaneously reducing the surface area due to sintering. Among the variations tested, hematite calcined at 250°C exhibited the most effective photo-Fenton catalytic activity for *para*-nitrophenol (PNP) degradation, offering an optimal balance between structural order and surface accessibility. System optimization revealed that degradation efficiency was highly dependent on catalyst dosage, H_2O_2 concentration, and UV irradiation time, with the best performance achieved at a Fe:H_2O_2 molar ratio of 1:3, moderate catalyst mass, and 120 minutes of UV exposure. The reaction system maintained high performance within a pH range of 3–6, demonstrating stability and environmental compatibility. Structural and spectroscopic analyses (XRD, FTIR) confirmed the material's post-reaction stability, while AAS results indicated minimal Fe leaching, suggesting good structural stability under the applied reaction conditions. These findings highlight α-Fe_2O_3 as a promising, low-cost, and reusable heterogeneous catalyst for photo-Fenton-based degradation under near-neutral conditions. Future studies should investigate catalyst reusability, performance in real wastewater matrices, and the contribution of photo-induced versus dark Fenton processes through appropriate control experiments.

Credit authorship contribution statement

Swastika Pitahaya Novianiti: Conceptualization, Methodology, Software, Data curation, Investigation, Visualization, Writing – Original draft, Writing – Reviewing & editing. **Endang Tri Wahyuni**: Conceptualization, Supervision, Methodology, Validation, Project administration, Resources, Writing – Review & editing. **Nurul Hidayat Aprilita**: Formal analysis, Supervision, Validation, Writing – Review & editing.

Declaration of competing interest

The authors declare that they have no known competing financial interests or personal relationships that could have appeared to influence the work reported in this paper.

Acknowledgment

This research was supported by funding from the Ministry of Education, Culture, Research, and Technology of the Republic of Indonesia [grant numbers 067/C3/DT.05.00/PL/2025]. The author gratefully acknowledges the support and guidance provided by academic supervisors and colleagues during the completion of this study.

Access to laboratory facilities and constructive feedback throughout the research process were essential and deeply appreciated.

References

[1] K. Tiar, A. Soualah, C. Bisio, M. Guidotti, Effect of Initial Solution pH on 4-Nitrophenol Oxidation Through Homogeneous/Heterogeneous Photo-Fenton Process Using Goethite/H_2O_2 System, J. Photochem. Photobiol. A Chem. 447 (2024) 115184. https://doi.org/10.1016/j.jphotochem.2023.115184.

[2] F. Li, K. Zhu, B. Liu, N. Wang, H. Liu, R. Chen, Comprehensive Effect of P-Nitrophenol Degradation in the Iron Oxide/Oxalate Suspension, Water, Air, Soil Pollut. 229 (2018) 91. https://doi.org/10.1007/s11270-018-3748-7.

[3] V.N. Lima, C.S.D. Rodrigues, Y.B. Brandão, M. Benachour, L.M. Madeira, Optimisation of the Degradation of 4-Nitrophenol by Fenton's Process, J. Water Process Eng. 47 (2022) 102685. https://doi.org/10.1016/j.jwpe.2022.102685.

[4] Y. Wu, R. Chen, H. Liu, Y. Wei, D. Wu, Feasibility and Mechanism of p-nitrophenol Decomposition in Aqueous Dispersions of Ferrihydrite and H_2O_2 under Irradiation, React. Kinet. Mech. Catal. 110 (2013) 87–99. https://doi.org/10.1007/s11144-013-0571-4.

[5] C.S.D. Rodrigues, R.A.C. Borges, V.N. Lima, L.M. Madeira, p-Nitrophenol Degradation by Fenton's Oxidation in a Bubble Column Reactor, J. Environ. Manag. 206 (2018) 774–785. https://doi.org/https://doi.org/10.1016/j.jenvman.2017.11.032.

[6] T. Liu, N. Chen, Y. Deng, F. Chen, C. Feng, Degradation of p-Nitrophenol by Nano-Pyrite Catalyzed Fenton Reaction with Enhanced Peroxide Utilization, RSC Adv. 10 (2020) 15901–15912. https://doi.org/10.1039/D0RA01177K.

[7] L. Clarizia, D. Russo, I. Di Somma, R. Marotta, R. Andreozzi, Homogeneous Photo-Fenton Processes at Near Neutral pH: A Review, Appl. Catal. B Environ. 209 (2017) 358–371. https://doi.org/10.1016/j.apcatb.2017.03.011.

[8] M. Ahmad, A.R.A. Aziz, S.A. Mazari, A.G. Baloch, S. Nizamuddin, Photocatalytic Degradation of Methyl Orange from Wastewater Using A Newly Developed Fe-Cu-Zn-ZSM-5 Catalyst, Environ. Sci. Pollut. Res. 27 (2020) 26239–26248. https://doi.org/10.1007/s11356-020-08940-9.

[9] K. O'Dowd, S.C. Pillai, Photo-Fenton Disinfection at Near Neutral pH: Process, Parameter Optimization and Recent Advances, J. Environ. Chem. Eng. 8 (2020) 104063. https://doi.org/10.1016/j.jece.2020.104063.

[10] J. Herney-Ramirez, M.A. Vicente, L.M. Madeira, Heterogeneous Photo-Fenton Oxidation with Pillared Clay-based Catalysts for Wastewater Treatment: A Review, Appl. Catal. B Environ. 98 (2010) 10–26. https://doi.org/10.1016/j.apcatb.2010.05.004.

[11] A. Barwal, R. Chaudhary, Effectiveness of Solar Photo-Fenton Process for Simultaneous Detoxification of Heavy Metals and Disinfection in Municipal Wastewater by Using Response Surface Method, Environ. Prog. Sustain. Energy 36 (2017) 448–459. https://doi.org/10.1002/ep.12486.

[12] A. Choquehuanca, J.G. Ruiz-Montoya, A. La Rosa-Toro Gómez, Discoloration of methylene blue at neutral pH by heterogeneous photo-Fenton-like reactions using crystalline and amorphous iron oxides, Open Chem. 19 (2021) 1009–1020. https://doi.org/10.1515/chem-2021-0077.

[13] M. Silva, J. Baltrusaitis, Destruction of emerging organophosphate contaminants in wastewater using the heterogeneous iron-based photo-Fenton-like process, J. Hazard. Mater. Lett. 2 (2021) 100012. https://doi.org/10.1016/j.hazl.2020.100012.

[14] E.T. Wahyuni, A. Sabrina, N.H. Aprilita, Enhancement of Fenton Performance at Near-Neutral pH by Using Ethylene Diamine Tetra Acetic Acid for Anionic Surfactant Removal from a Laundry Wastewater, Key Eng. Mater. 920 (2022) 57–62. https://doi.org/10.4028/p-665217.

[15] L. Zhou, L. Wang, J. Zhang, J. Lei, Y. Liu, Well-Dispersed Fe_2O_3 Nanoparticles on g-C_3N_4 for Efficient and Stable Photo-Fenton Photocatalysis under Visible-Light Irradiation, Eur. J. Inorg. Chem. 2016 (2016) 5387–5392. https://doi.org/10.1002/ejic.201600959.

[16] T. Guo, K. Wang, G. Zhang, X. Wu, A novel α-Fe_2O_3@g-C_3N_4 Catalyst: Synthesis Derived from Fe-based MOF and its Superior Photo-Fenton Performance, Appl. Surf. Sci. 469 (2019) 331–339. https://doi.org/10.1016/j.apsusc.2018.10.183.

[17] D. Liu, C. Li, T. Ni, R. Gao, J. Ge, F. Zhang, W. Wu, J. Li, Q. Zhao, 3D Interconnected Porous g-C_3N_4 Hybridized with Fe_2O_3 Quantum Dots for Enhanced Photo-Fenton Performance, Appl. Surf. Sci. 555 (2021) 149677. https://doi.org/10.1016/j.apsusc.2021.149677.

[18] H. Zhao, C. Tian, J. Mei, S. Yang, P.K. Wong, Faster Electron Injection and Higher Interface Reactivity in g-C_3N_4/Fe_2O_3 Nanohybrid for Efficient Photo-Fenton-like Activity toward Antibiotics Degradation, Environ. Res. 195 (2021) 110842. https://doi.org/10.1016/j.envres.2021.110842.

[19] X. Qian, M. Ren, Y. Zhu, D. Yue, Y. Han, J. Jia, Y. Zhao, Visible Light Assisted Heterogeneous Fenton-Like Degradation of Organic Pollutant via α-FeOOH/Mesoporous Carbon Composites, Environ. Sci. Technol. 51 (2017) 3993–4000. https://doi.org/10.1021/acs.est.6b06429.

[20] J. Hu, J. Li, J. Cui, W. An, L. Liu, Y. Liang, W. Cui, Surface Oxygen Vacancies enriched FeOOH/Bi_2MoO_6 Photocatalysis-Fenton Synergy Degradation of Organic Pollutants, J. Hazard. Mater. 384 (2020) 121399. https://doi.org/10.1016/j.jhazmat.2019.121399.

[21] L. Xu, J. Wang, Fenton-like Degradation of 2,4-Dichlorophenol Using Fe_3O_4 Magnetic Nanoparticles, Appl. Catal. B Environ. 123–124 (2012) 117–126. https://doi.org/10.1016/j.apcatb.2012.04.028.

[22] L. Xu, J. Wang, Magnetic Nanoscaled Fe_3O_4/CeO_2 Composite as an Efficient Fenton-Like Heterogeneous Catalyst for Degradation of 4-Chlorophenol, Environ. Sci. Technol. 46 (2012) 10145–10153. https://doi.org/10.1021/es300303f.

[23] P.K. Boruah, B. Sharma, I. Karbhal, M. V. Shelke, M.R. Das, Ammonia-modified Graphene Sheets Decorated with Magnetic Fe_3O_4 Nanoparticles for the Photocatalytic and Photo-Fenton Degradation of Phenolic Compounds under Sunlight Irradiation, J. Hazard. Mater. 325 (2017) 90–100. https://doi.org/10.1016/j.jhazmat.2016.11.023.

[24] R. Saleh, A. Taufik, Degradation of Methylene Blue and Congo-Red Dyes Using Fenton, Photo-Fenton, Sono-Fenton, and Sonophoto-Fenton Methods in the Presence of Iron(II,III) Oxide/Zinc Oxide/Graphene (Fe_3O_4/ZnO/Graphene) Composites, Sep. Purif. Technol. 210 (2019) 563–573. https://doi.org/10.1016/j.seppur.2018.08.030.

[25] X. Li, K. Cui, Z. Guo, T. Yang, Y. Cao, Y. Xiang, H. Chen, M. Xi, Heterogeneous Fenton-like Degradation of Tetracyclines Using Porous Magnetic Chitosan Microspheres as An Efficient Catalyst Compared with Two Preparation Methods, Chem. Eng. J. 379 (2020) 122324. https://doi.org/10.1016/j.cej.2019.122324.

[26] R. Wang, Y. Chu, H. Zhang, Comprehensive Evaluation of the Catalytic Activity of alpha-Ferric Oxide

in Photocatalysis, Fenton-like and Photo-Fenton Systems for Organics Degradation: Performance and in-depth Mechanism Consideration, J. Environ. Chem. Eng. 12 (2024) 112479. https://doi.org/10.1016/j.jece.2024.112479.

[27] L. Guo, F. Chen, X. Fan, W. Cai, J. Zhang, S-doped α-Fe2O3 as a Highly Active Heterogeneous Fenton-like Catalyst towards the Degradation of Acid Orange 7 and Phenol, Appl. Catal. B Environ. 96 (2010) 162–168. https://doi.org/10.1016/j.apcatb.2010.02.015.

[28] K. Tiar, A. Soualah, C. Bisio, S. Marchesi, V. Pappalardo, S. Econdi, M. Guidotti, Tuning iron loading and specific surface area in iron-containing clays for the oxidative photodegradation of 4-nitrophenol, Appl. Catal. A Gen. 707 (2025). https://doi.org/10.1016/j.apcata.2025.120522.

[29] S.-P. Sun, A.T. Lemley, p-Nitrophenol Degradation by a Heterogeneous Fenton-like Reaction on Nano-Magnetite: Process Optimization, Kinetics, and Degradation Pathways, J. Mol. Catal. A Chem. 349 (2011) 71–79. https://doi.org/10.1016/j.molcata.2011.08.022.

[30] J. Xu, Q. Ma, W. Feng, X. Zhang, Q. Lin, C. You, X. Wang, Removal of Methyl Orange from Water by Fenton Oxidation of Magnetic Coconut-Clothed Biochar, RSC Adv. 12 (2022) 24439–24446. https://doi.org/10.1039/d2ra03545f.

[31] A.R. Chakraborty, F.T. Zohora Toma, K. Alam, S.B. Yousuf, K.S. Hossain, Influence of Annealing Temperature on Fe_2O_3 Nanoparticles: Synthesis Optimization and Structural, Optical, Morphological, and Magnetic Properties Characterization for Advanced Technological Applications, Heliyon 10 (2024) e40000. https://doi.org/10.1016/j.heliyon.2024.e40000.

[32] M.K. Ghosh, G.E.J. Poinern, T.B. Issa, P. Singh, Arsenic Adsorption on Goethite Nanoparticles Produced through Hydrazine Sulfate Assisted Synthesis Method, Korean J. Chem. Eng. 29 (2012) 95–102. https://doi.org/10.1007/s11814-011-0137-y.

[33] S. Guo, G. Zhang, J. Wang, Photo-Fenton Degradation of Rhodamine B using Fe_2O_3-Kaolin as Heterogeneous Catalyst: Characterization, Process Optimization and Mechanism, J. Colloid Interface Sci. 433 (2014) 1–8. https://doi.org/10.1016/j.jcis.2014.07.017.

[34] M. Habran, P.I. Pontón, L. Mancic, O. Pandoli, K. Krambrock, M.E.H. Maia, S. Letichevsky, A.M.L.M. Costa, E. Morgado, B.A. Marinkovic, Journal of Photochemistry & Photobiology A : Chemistry Visible

Light Sensitive Mesoporous Nanohybrids of Lepidocrocite-like Ferrititanate Coupled to a Charge Transfer Complex : Synthesis, Characterization and Photocatalytic Degradation of NO, J. Photochem. Photobiol. A Chem. 365 (2018) 133–144. https://doi.org/https://doi.org/10.1016/j.jphotochem.2018.07.038.

[35] A. Hakim, M.A. Yarmo, T.S. Marliza, M.N.A. Tahari, W.Z. Samad, M.R. Yusop, M.W.M. Hisham, N. Dzakaria, The Influence of Calcination Temperature On Iron Oxide (α-Fe_2O_3) Towards CO_2 Adsorption Prepared By Simple Mixing Method, Malaysian J. Anal. Sci. 20 (2016) 1286–1298. https://doi.org/10.17576/mjas-2016-2006-07.

[36] M. Mohammadikish, Hydrothermal Synthesis, Characterization and Optical Properties of Ellipsoid Shape α-Fe_2O_3 Nanocrystals, Ceram. Int. 40 (2014) 1351–1358. https://doi.org/10.1016/j.ceramint.2013.07.016.

[37] M. Dutt, K. Suhasini, A. Ratan, J. Shah, R.K. Kotnala, V. Singh, Mesoporous Silica Mediated Synthesis of α-Fe_2O_3 Porous Structures and their Application as Humidity Sensors, J. Mater. Sci. Mater. Electron. 29 (2018) 20506–20516. https://doi.org/10.1007/s10854-018-0186-7.

[38] W. Salama, M. El Aref, R. Gaupp, Spectroscopic Characterization of Iron Ores Formed in Different Geological Environments Using FTIR, XPS, Mössbauer Spectroscopy and Thermoanalyses, Spectrochim. Acta Part A Mol. Biomol. Spectrosc. 136 (2015) 1816–1826. https://doi.org/10.1016/j.saa.2014.10.090.

[39] Y. Wang, Y. Gao, L. Chen, H. Zhang, Goethite as an efficient heterogeneous Fenton catalyst for the degradation of methyl orange, Catal. Today 252 (2015) 107–112. https://doi.org/10.1016/j.cattod.2015.01.012.

[40] M. Zain, K.A. Yasin, S. Haq, W. Rehman, S.U. Din, S. Shujaat, A. Syed, M.K. Hossain, B.A. Paray, J. Razzokov, A. Samad, Effect of Calcination Temperature Induced Structural Modifications on the Photocatalytic Efficacy of Fe_2O_3-ZrO_2 Nanostructures: Mechanochemical Synthesis, RSC Adv. 14 (2024) 15085–15094. https://doi.org/10.1039/d4ra01944j.

[41] S.S. Abdullahi, S. Güner, Y. Koseoglu, I.M. Musa, B.I. Adamu, M.I. Abdulhamid, Simple Method for the Determination of Band Gap of A Nanopowdered Sample Using Kubelka Munk Theory, J. Niger. Assoc. Math. Phys. 35 (2016) 241–264. https://www.researchgate.net/profile/Bala-

Adamu/publication/305810656_Simple_Method_For_The_Determination_of_Band_Gap_of_a_Nanopowdered_Sample_Using_Kubelka_Munk_Theory/links/57a2f3e408aeb16048366032/Simple-Method-For-The-Determination-of-Band-Gap-of-a-Na.

[42] A. Saidani, R. Boudraa, K. Fendi, L. Benouadah, A. Benabbas, A. Djermoune, S. Salvestrini, J.-C. Bollinger, A.A. Alayyaf, L. Mouni, Effect of Calcination Temperature on the Photocatalytic Activity of Precipitated ZnO Nanoparticles for the Degradation of Rhodamine B Under Different Light Sources, Water 17 (2024) 32. https://doi.org/10.3390/w17010032.

[43] M. Hojamberdiev, G. Zhu, A. Eminov, K. Okada, Template-Free Hydrothermal Synthesis of Hollow α-FeOOH Urchin-Like Spheres and Their Conversion to α-Fe_2O_3 Under Low-Temperature Thermal Treatment in Air, J. Clust. Sci. 24 (2013) 97–106. https://doi.org/10.1007/s10876-012-0522-7.

[44] Y. Zhu, Q. Xie, F. Deng, Z. Ni, Q. Lin, L. Cheng, X. Chen, R. Qiu, R. Zhu, The differences in heterogeneous Fenton catalytic performance and mechanism of various iron minerals and their influencing factors: A review, Sep. Purif. Technol. 325 (2023) 124702. https://doi.org/10.1016/j.seppur.2023.124702.

[45] Y. Li, Z. Lv, S. Zhang, Y. Zhang, S. Wu, R. Liu, Controlled Fabrication and Characterization of α-FeOOH Nanorods, J. Inorg. Organomet. Polym. Mater. 32 (2022) 1400–1408. https://doi.org/10.1007/s10904-021-02190-z.

[46] S.R. Pouran, A.R.A. Aziz, W.M.A.W. Daud, Review on the Main Advances in Photo-Fenton Oxidation System for Recalcitrant Wastewaters, J. Ind. Eng. Chem. 21 (2015) 53–69. https://doi.org/10.1016/j.jiec.2014.05.005.

[47] W.S. Hamd, J. Dutta, Heterogeneous Photo-Fenton Reaction and its Enhancement upon Addition of Chelating Agents, in: Nanomater. Detect. Remov. Wastewater Pollut., Elsevier, 2020: pp. 303–330. https://doi.org/10.1016/B978-0-12-818489-9.00011-6.

[48] Y. Ahmed, Z. Yaakob, P. Akhtar, Degradation and mineralization of methylene blue using a heterogeneous photo-Fenton catalyst under visible and solar light irradiation, Catal. Sci. Technol. 6 (2016) 1222–1232. https://doi.org/10.1039/c5cy01494h.

[49] H. Ghazzaf, B. Nechchadi, A. Jouali, A. Salhi, M. El Krati, S. Tahiri, Synthesis of Heterogeneous

Photo-Fenton Catalyst from Iron Rust and its Application to Degradation of Acid Red 97 in Aqueous Medium, J. Environ. Chem. Eng. 10 (2022). https://doi.org/10.1016/j.jece.2022.107570.

[50] A.N. Soon, B.H. Hameed, Heterogeneous Catalytic Treatment of Synthetic Dyes in Aqueous Media Using Fenton and Photo-Assisted Fenton Process, Desalination 269 (2011) 1–16. https://doi.org/10.1016/j.desal.2010.11.002.

[51] X. Liu, H.-L. Liu, K.-P. Cui, Z.-L. Dai, B. Wang, X. Chen, Heterogeneous Photo-Fenton Removal of Methyl Orange Using the Sludge Generated in Dyeing Wastewater as Catalysts, Water 14 (2022) 629. https://doi.org/10.3390/w14040629.

[52] M. Mishra, D.M. Chun, α-Fe2O3 as a photocatalytic material: A review, Appl. Catal. A Gen. 498 (2015) 126–141. https://doi.org/10.1016/j.apcata.2015.03.023.

[53] N. Thomas, D.D. Dionysiou, S.C. Pillai, Heterogeneous Fenton Catalysts: A Review of Recent Advances, J. Hazard. Mater. 404 (2021) 124082. https://doi.org/10.1016/j.jhazmat.2020.124082.

[54] L. Demarchis, M. Minella, R. Nisticò, V. Maurino, C. Minero, D. Vione, Photo-Fenton reaction in the presence of morphologically controlled hematite as iron source, J. Photochem. Photobiol. A Chem. 307–308 (2015) 99–107. https://doi.org/10.1016/j.jphotochem.2015.04.009.